



Provided by the author(s) and University of Galway in accordance with publisher policies. Please cite the published version when available.

Title	A precipitate evolution-based continuum damage mechanics model of creep behaviour in welded 9Cr steel at high temperature
Author(s)	Ó Murchú, Cathal; Leen, Sean B.; O'Donoghue, Padraic E.; Barrett, Richard A.
Publication Date	2018-04-04
Publication Information	Ó Murchú, C., Leen, S., O'Donoghue, P., & Barrett, R. (2019). A precipitate evolution-based continuum damage mechanics model of creep behaviour in welded 9Cr steel at high temperature. <i>Proceedings of the Institution of Mechanical Engineers, Part L: Journal of Materials: Design and Applications</i> , 233(1), 39–51. <a href="https://doi.org/10.1177/1464420718762607">https://doi.org/10.1177/1464420718762607</a>
Publisher	SAGE Publications
Link to publisher's version	<a href="https://doi.org/10.1177/1464420718762607">https://doi.org/10.1177/1464420718762607</a>
Item record	<a href="http://hdl.handle.net/10379/15630">http://hdl.handle.net/10379/15630</a>
DOI	<a href="http://dx.doi.org/10.1177/1464420718762607">http://dx.doi.org/10.1177/1464420718762607</a>

Downloaded 2024-04-26T05:55:50Z

Some rights reserved. For more information, please see the item record link above.



# **A precipitate evolution based continuum damage mechanics model of creep behaviour in welded 9Cr steel at high temperature**

C. Ó Murchú<sup>1,2</sup>, S.B. Leen<sup>2,3#</sup>, P.E. O'Donoghue<sup>1,2,\*</sup>, R.A. Barrett<sup>2,3,#</sup>

<sup>1</sup>Civil Engineering, College of Engineering and Informatics, NUI Galway, Ireland.

<sup>2</sup>Ryan Institute for Environmental, Marine and Energy Research, NUI Galway, Ireland.

<sup>3</sup>Mechanical Engineering, College of Engineering and Informatics, NUI Galway, Ireland.

**\*Corresponding author:** Prof. Padraic O'Donoghue

**Email:** padraic.odonoghue@nuigalway.ie

**Tel.:** +353 91 492 214

**#Joint senior authors.**

**Keywords:** Precipitates, weldments, 9Cr steel, damage mechanics, lifetime prediction.

## **Abstract:**

A multiaxial, physically-based, continuum damage mechanics methodology for creep of welded 9Cr steels, is presented, incorporating a multiple precipitate type state variable which simulates the effects of strain- and temperature-induced coarsening kinematics. Precipitate volume fraction and initial diameter for carbide and carbo-nitride precipitate types are key microstructural variables controlling time to failure in the model. The heat affected zone material is simulated explicitly utilising measured microstructural data, allowing detailed investigation of failure mechanisms. Failure is shown to be controlled by a combination of microstructural degradation and Kachanov type damage for the formation and growth of creep cavities. Comparisons with experimental data demonstrate the accuracy of this model for P91 material.

## 1. Introduction

### *1.1. Background*

A significant reduction in CO<sub>2</sub> emissions from fossil fuel power plant is urgently required to limit the effects of global warming [1]. Key methods of reducing emissions include increased firing temperature, increased operating pressure and the greater use of renewable energy sources in electricity generation. However, the inclusion of intermittent renewable sources to the electricity grid has led to more frequent start up and shut down cycles in power plants [2]. This cycling can lead to thermo-mechanical fatigue (TMF) occurring within plant components, giving rise to unexpected failures. Thus, enhanced combined creep-fatigue loading is predicted to significantly decrease the plant operational life.

9Cr steels are currently utilized for plant components experiencing these TMF and elevated temperature loads. Failure has predominantly been observed within weldments of these steels, specifically in the heat-affected zone (HAZ) region adjacent to the parent material. The heterogeneous microstructure of the HAZ region causes strain localisation due to material property gradients generated by the welding procedure. While extensive characterisation work has been performed on the microstructure of the HAZ regions, applying this knowledge to predictive models has received less attention due to the complexities of the microstructural evolution during creep.

### *1.2. Microstructure of parent material*

The 9Cr steels owe their high creep strength to their hierarchical microstructure [3]. This consists of prior austenite grains, containing packets and blocks, each having crystal misorientation of greater than 5°; i.e. high angle boundaries. Blocks are subdivided further into martensitic laths and regions of high dislocation density demarcate the boundaries of the laths. Precipitates are dispersed throughout the microstructure of the steels including (i)

$M_{23}C_6$  carbides, where M represents either Cr, Fe or Mo, and (ii) MX, which are Nb or V carbonitrides.  $M_{23}C_6$  carbides are observed predominantly on lath boundaries and MX precipitates are dispersed throughout the microstructure. Figure 1 shows a schematic of the microstructure of 9Cr steels, with details of these features described elsewhere e.g. [4,5]. It should be noted that during service, this elongated tempered lath martensite microstructure is rearranged to a structure of gradually coarsening subgrains, with boundaries containing carbides which also experience coarsening.

The primary obstructions to dislocation movement within the steel are these nano-scale precipitates and microstructural boundaries. Dislocations become trapped by these obstacles and are no longer able to transfer plastic deformation through the microstructure. The spacing between individual obstacles governs this strengthening mechanism in an Orowan type relationship [6]. Therefore, a key microstructural variable in this approach is the average spacing of obstacles to dislocation movement and its evolution during creep exposure. This spacing is assumed here to be dominated by precipitate coarsening kinematics.

Evolution of the microstructure during high temperature creep exposure has been well documented for these materials [7,8]. This deterioration consists of precipitate coarsening, formation of new intermetallic phases (e.g. Laves phase particles) and cavitation damage. The requirement to simulate the contributions of both  $M_{23}C_6$  and MX precipitates to creep strength is demonstrated in the continuum damage mechanics (CDM) creep model of Ó Murchú et al. [5], where an 80% reduction in MX volume fraction is predicted to reduce creep life by a factor of 6.  $M_{23}C_6$  precipitates are known to be less thermally stable than MX precipitates during creep, along with experiencing enhanced strain-induced coarsening [8,9,10]. The solubility of alloying elements within the matrix dominates the rate of particle coarsening. The high coarsening rate of  $M_{23}C_6$  carbides compared to MX precipitates, can be

attributed to the solubility of Cr and Mo, compared to that of V and Nb in the matrix [8,9]. While not explicitly modelled in this work, it is important to highlight the driving factors for the differences in behaviour of these two families of precipitates.

Cavitation damage is the process of vacancy diffusion through the crystal lattice to conglomerate into large voids leading to cavities, principally formed at the grain boundaries and at triple points [11]. Lee et al. [12] proposed, a threshold diameter of 250 nm for  $M_{23}C_6$  carbides to cause enhanced cavity nucleation, based on their observations of welded 9Cr steel creep specimens.

New intermetallic phases such as Laves phase and Z-phase particles also form during high temperature creep of 9Cr steels. Laves phase forms near  $M_{23}C_6$  precipitates and leach Mo and W from the matrix during creep, subsequently coarsening to larger diameters than the  $M_{23}C_6$  carbides, as observed by Panait et. al. [7]. Z-phase are complex CrVN or CrNbV nitrides, which remove MX precipitates from the metal matrix, severely reducing the life expectancy of 9Cr components. High chromium content accelerates the formation of Z-phase precipitates which are far larger than the MX type [13], reducing the pinning effect. Z-phase typically forms in parent material after long term creep exposure, e.g. after more than 100,000 hours at 600 °C [13]. However they may form more rapidly within the weld metal depending on consumable composition, especially in the case of elevated levels of nitrogen [14].

### *1.3. Microstructure of weld material*

Examinations of welded sections prior to post weld heat treatment (PWHT) show columnar grains, formed due to directional solidification after welding. Lath martensite is formed within this material during cooling and high dislocation densities are observed within the laths and lower volume fractions of carbides have been observed [15,16]. Precipitate formation within the weld is attributed to auto tempering due to additional heating of

individual weld beads during multi-pass welding. During PWHT, carbides and precipitates form in greater volumes and laths evolve into subgrains [16].

#### *1.4. Microstructure of HAZ regions*

The HAZ contains several sub regions, known as coarse grained, fine grained and inter-critical HAZ (ICHAZ) regions, formed due to heat exposure during the weld procedure. Figure 2 depicts a schematic of the weld zone regions, showing their positions relative to the fusion line.

Most failures have occurred within the ICHAZ region of a weldment and so the microstructure of this region is particularly important. Lee et al. [12] report increased precipitate diameters for both  $M_{23}C_6$  and MX precipitates within the ICHAZ region after PWHT for a 9Cr steel and similar results are observed by Paul et al. [15] and Vijayalakshmi et al. [17]. Vijayalakshmi et al. reported a significantly reduced volume fraction of  $M_{23}C_6$  precipitates in the ICHAZ compared to the parent material. This is due to partial dissolution and re-precipitation of the carbide during the welding process. For the purposes of this paper, the modelled HAZ material parameters are based on available ICHAZ literature data wherever possible. Otherwise averaged data for the entire HAZ were employed.

This paper implements a multiple precipitate type, CDM based model for 9Cr steels, specifically focusing on the weldment region. A rigorous parameter identification methodology is presented along with validation against test data.

## **2. Multi-precipitate type modelling methodology**

The following is a brief discussion of the hyperbolic sine-based CDM model implemented within an explicit creep user subroutine for use with the non-linear, finite element code, Abaqus<sup>TM</sup>. An explicit integration scheme was employed, requiring the use of a converged

time increment. A creep strain error tolerance, of  $6.66 \times 10^{-6}$  [18] is used. Mesh refinement studies were performed to ensure that results were mesh independent. The cross-weld (CW) specimen was modelled as a 2D axisymmetric bar in Abaqus<sup>TM</sup>, to reduce computational time.

The hyperbolic sine flow rule has been demonstrated by Barrett et al. [4] to give agreement with experimental data for 9Cr steels tested at both high and low stress regimes. The present implementation includes a multiple precipitate strain- and temperature-induced coarsening state variable,  $D_P$ , with details on the derivation presented in Ó Murchú et al. [5]. The creep strain rate is defined following the approach of Dyson and Osgerby [19], Perrin and Hayhurst [20] and Hyde et al. [21] for precipitate strengthened steels as follows:

$$\dot{\epsilon}_{ij}^{cr} = \frac{3}{2} \frac{S_{ij}}{\sigma_{eq}} \dot{\epsilon}_0 \exp\left(\frac{-\Delta F}{k_B T}\right) \sinh\left[\frac{\sigma_{eq}(1-H)}{\sigma_0(1-D_P)(1-D_{CV})}\right], \quad (1)$$

In this equation,  $S_{ij}$  is deviatoric stress tensor,  $\sigma_{eq}$  is equivalent (von Mises) stress and  $\dot{\epsilon}_0$  is a temperature-independent constant. Temperature-dependence is achieved via an Arrhenius type term with  $\Delta F$  as Helmholtz free energy ( $5.978 \times 10^{-19}$  J),  $k_B$  as the Boltzmann constant ( $1.38 \times 10^{-23}$  m<sup>2</sup> kg s<sup>-2</sup> K<sup>-1</sup>) and  $T$ , absolute temperature. Primary hardening is represented via the state variable,  $H$ , while  $D_{CV}$  is the state variable representing cavitation damage, with a value ranging from zero initially to a value of unity at failure. The Helmholtz free energy term was identified from the work of Oruganti et al. [22] on precipitate and subgrain kinematics at various temperatures in a 9Cr steel, it is assumed constant for all materials here.

The creep constant  $\sigma_0$  is based on the activation volume approach of Dyson [23]:

$$\sigma_0 = \frac{Mk_B T}{b^2 \lambda_{ob}}, \quad (2)$$

where  $M$  is the Taylor factor (2.9 for body centre cubic (BCC) materials),  $b$  is the magnitude of the Burgers vector (taken here to be 0.248 nm, the value for BCC iron), and  $\lambda_{ob}$  is obstacle spacing. An equivalent obstacle spacing is defined, based on contributions due to spacing of precipitates, grains, laths and dislocation density [24], as follows:

$$\frac{1}{\lambda_{ob}} = \sqrt{\frac{\lambda_c^2 + \lambda_m^2}{\lambda_c^2 \lambda_m^2}} + \frac{1}{w} + \frac{1}{d_g} + \sqrt{\rho}, \quad (3)$$

$\lambda_c$  and  $\lambda_m$  are particle spacings for  $M_{23}C_6$  and MX, respectively,  $w$  is lath width,  $d_g$  is prior austenite grain size and  $\rho$  is dislocation density. Precipitate spacing is calculated based on the volume fraction of precipitates in a single unit cell, and the diameter of a given precipitate:

$$\lambda_i = d_i \left[ \left( \frac{\pi}{6f_i} \right)^{1/3} - 1 \right], \quad (4)$$

where  $d$  is the precipitate diameter,  $f$  is volume fraction and the index  $i$  is either c or m representing  $M_{23}C_6$  or MX precipitates, respectively. Precipitate diameter is evaluated based on the strain and temperature induced coarsening equation developed by Taneike et al. [9]:

$$d_i^3 - d_{i,0}^3 = K_i t + \Phi_i \varepsilon_{eq}^{cr}, \quad (5)$$

where  $d_{i,0}$  is initial precipitate diameter,  $K_i$  is thermal coarsening rate,  $\Phi_i$  is strain-induced coarsening parameter,  $t$  is current creep exposure time and  $\varepsilon_{eq}^{cr}$  is equivalent creep strain. Utilising the precipitate spacing and diameter, Equations (4) and (5) respectively, the precipitate state variable, is defined as follows [5]:

$$\dot{D}_p = \frac{d_{1,0}^2 d_{2,0}^2}{3(d_{1,0}^2 B_1 + d_{2,0}^2 B_2)} \left( \frac{B_1}{d_2^5} (K_2 + \Phi_2 \dot{\epsilon}_{eq}^{cr}) + \frac{B_2}{d_1^5} (K_1 + \Phi_1 \dot{\epsilon}_{eq}^{cr}) \right) \frac{1}{(1 - D_p)}, \quad (6)$$

where  $\dot{\epsilon}_{eq}^{cr}$  is the equivalent creep strain rate and  $B_i$  is a constant related to the precipitate spacing term by:

$$B_i = \left( \frac{\lambda_i}{d_i} \right)^2 = \left[ \left( \frac{\pi}{6f_i} \right)^{1/3} - 1 \right]^2, \quad (7)$$

The primary hardening term of Equation (1) is from the work of Hayhurst [20], who developed a primary creep CDM model for a 0.5Cr-0.5Mo-0.25V steel, as follows:

$$\dot{H} = \frac{h \dot{\epsilon}_{eq}^{cr}}{\sigma_{eq}} \left( 1 - \frac{H}{H^*} \right), \quad (8)$$

where  $h$  is primary hardening rate and  $H^*$  is a primary hardening limit value. This model captures the effect of the initial strain hardening within the material due to loss of mobile dislocations to entanglements and pile ups at boundaries.

A Kachanov type damage law is utilised to include the effect of cavity growth via the loss of load bearing section within a material. The inclusion of a triaxiality term for multi-axial stress states captures the observed phenomenon of cracking occurring within regions of high stress triaxiality, as follows:

$$\dot{D}_{CV} = C \dot{\epsilon}_{eq}^{cr} \left( \frac{\sigma_1}{\sigma_{eq}} \right)^v, \quad (9)$$

where  $C$  is the cavitation constant,  $\sigma_1$  is the maximum principal stress and  $v$  is the triaxiality exponent. This is particularly relevant for welded connections as the material property

mismatch within the weld region generates localised areas of high triaxiality as demonstrated by Watanabe et. al. [25].

### 3. Parameter identification and numerical modelling

In the model implemented here, the parent metal (PM), weld metal (WM) and HAZ are considered as three separate materials with different sets of properties. As an initial approximation, the HAZ is assumed to be a single material. For each material, there are seventeen input parameters that need to be determined. Twelve of these are microstructural and the remaining five are the pre-exponential constant,  $\dot{\epsilon}_0$ , the primary hardening rate and limit,  $h$  and  $H^*$ , respectively, the cavitation term,  $C$ , and the triaxiality exponent,  $\nu$ . All constants are identified either directly or indirectly from published data. The following sections describe the process of identification of these parameters.

#### 3.1. Identification of creep constants

The model has been calibrated in previous work for a P91 parent material in the temperature regime 600 °C to 650 °C [5]. The steady state creep constants were identified based on minimum strain rate (MSR) data from Hyde et al. [26] using the following equations:

$$MSR = \dot{\epsilon}_0 \exp\left(\frac{-\Delta F}{k_B T}\right) \sinh\left[\frac{\sigma_{eq}}{\sigma_0}\right], \quad (10)$$

A least squares optimisation methodology was employed to identify  $\dot{\epsilon}_0$  and  $\sigma_0$ . Figure 3 shows that the equation captures the effect of stress for both the parent and weld metal with the MSR experimental data coming from creep indentation testing. The benefit of utilising a hyperbolic sine based flow rule is demonstrated in Figure 4, which shows agreement between

a predicted MSR from Equation (10) and test data from Haney et al. [27] for P91 parent material across a wide range of stress at 600 °C and 650 °C. The model calibration was performed for Bar 257 (a variant of P91 with an increased aluminium concentration) parent material at 650 °C [5], and a 9Cr weld metal with test data obtained from the literature [4]. Table 1 shows the identified creep constants for the three materials, including primary hardening and cavitation constants.

### *3.2. Calibration of primary hardening and cavitation constants*

The identification of primary hardening variables,  $h$  and  $H^*$ , and the cavitation constant,  $C$ , from measured tensile creep strain curves for P91 parent materials, utilising an automated least squares optimisation technique, has been described previously [5]. Figure 5 shows the corresponding identification of these three parameters for the weld material based on the experimental work of Agywaka [28], at 650 °C at 93 MPa and 100 MPa. The triaxiality exponent,  $\nu$ , was identified utilising the finite element methodology developed by Hyde et al. [21]. A range of exponent values were selected; based on the results of Hyde et al. [21] for a single precipitate type model, to calculate the corresponding time to failure. The calibration was performed for a net section nominal stress of 93 MPa at 650 °C.

### *3.3. Extraction of HAZ creep strain time data*

Measured test data is available for the weld and parent materials, but not for the HAZ material; thus, to obtain the HAZ creep response for identification of HAZ creep constants, a strain compatibility analysis of a CW specimen is employed. Figure 6 shows a schematic gage length of a three-material CW creep test specimen, as used by Hyde et al. [26] and Agywaka [28]. A creep strain curve can be extracted for the HAZ region using the strain compatibility approach suggested by Spigarelli and Quadrini [29], as follows:

$$\varepsilon_{HAZ} = \frac{1}{L_{HAZ}} (\varepsilon_{CW}L_{CW} - \varepsilon_{WM}L_{WM} - \varepsilon_{PM}L_{PM}), \quad (11)$$

where  $L_{HAZ}$ ,  $L_{WM}$ ,  $L_{CW}$  and  $L_{PM}$  are the representative lengths of the CW specimen shown in Figure 6 and defined in Table 2.  $\varepsilon_{HAZ}$ ,  $\varepsilon_{WM}$ ,  $\varepsilon_{CW}$  and  $\varepsilon_{PM}$ , are the corresponding creep strains in these regions. The CW, WM and PM responses are available from [21] and [28] as shown in Figure 7, for a stress of 93 MPa at 650 °C and the HAZ response is identified here using the latter equation. Clearly, the HAZ gives a significantly higher creep rate and strain accumulation than the CW, WM and PM. Figure 8 shows a comparison between the inferred HAZ response (via Equation 12) and the model predictions, demonstrating the capability of the model to represent the HAZ secondary creep response and rupture time. An elastic modulus of 110 GPa at 650 °C was assumed for each material [30].

#### *3.4. Selection of microstructural inputs*

Details of the parent material microstructure inputs are available previously [5].  $M_{23}C_6$  initial diameters for the weld were selected based on the measurements of Lee et al. [12] and Arivazhagan et al. [16] on welded 9Cr steels. Lee et al. investigated the microstructural degradation during creep of the HAZ material, concluding that coarsened  $M_{23}C_6$  precipitates and a mixture of soft and hard ferrite grains within the ICHAZ lead to Type IV failure. Arivazhagan et al. investigated the effect of Nb and V on the toughness of 9Cr weld material post weld. Four welds with varying content of Nb and V were subjected to Charpy V-notch impact testing, showing that a reduction of Nb and V increased the toughness of the weldment. Transmission electron microscopy (TEM) images allowed the estimation of  $M_{23}C_6$  precipitate size.

The HAZ precipitate diameters were selected based on the mean of measurements from TEM observations performed by Gaffard [31], Watanabe et al [25], Lee et al. [12] and

Vijayalakshmi et al. [17] on ICHAZ regions of welded P91 materials. Gaffard noted a factor of two increase between the PM and ICHAZ  $M_{23}C_6$  precipitate diameter, after post weld heat treatment. Watanabe et al. [25] noted that this precipitate family experienced a qualitatively larger coarsening within the HAZ region. Lee et al. [12] published values for both  $M_{23}C_6$  and MX precipitate families based on measurements performed on sections increasingly further from the fusion line, capturing the diameter differences between WM, HAZ and PM regions. Milović et al. [32] observed decreased concentrations of MX precipitates within the ICHAZ, when investigating the reduced hardness occurring within this region, but did not measure precipitate diameters in the same manner as Lee et al. [12] or Gaffard [31]. El-Azim et al. [33] observed MX precipitates of a similar size to those observed by Lee et al. [12] in a post weld heat treated P91 HAZ material. Precipitates within the HAZ region form during post weld heat treatment or in some cases during multi-pass welding, where auto-tempering can occur due to repeated heating from later passes.

Precipitate volume fraction data for the HAZ region was obtained from the work of Vijayalakshmi et al. [17], showing significantly reduced volume fractions within the sub-regions of the HAZ compared with parent material. Limited data is available for the precipitate volume fractions within the weld material of a welded connection, Spigarelli and Quadrini [29] note that, during the rapid cooling of the weld and HAZ, new precipitates do not form. Rather existing precipitates coarsen rapidly leading to a low volume fraction of precipitates in these regions. Barbadikar et al. [34] highlighted that an increase in normalising and tempering temperatures leads to a decrease in area fraction and an increase in precipitate diameter respectively for a tempering temperature increase from 740 °C to 780 °C. Multi-pass welding causes high temperature tempering, potentially reducing precipitate area fraction further. Paul et al. [15] reported no carbides within the weld zone for a P91 multi-pass weld with five weld layers laid using twelve torch passes per layer. Microstructural

characterization results were presented for the upper layer of weld material, farthest from the HAZ material i.e. pure weld material. This material, upon inspection after cooling, had not formed significant volume fraction of either precipitate families.

Elongated narrow prior austenite grains have been reported for the weld material, due to rapid directional solidification post weld; grain size data was obtained from the work of Paul et al. [15], Vijayalakshmi et al. [17] and Vivier et al. [35]. Similar investigations of the HAZ region were performed by El-Azim et al. [33], Paul et al, and Vivier et al. to measure grain size in this region of welded 9Cr after PWHT. Lath widths were also presented for the weld and HAZ materials by Paul et al [15], Vijayalakshmi et al. (weld and HAZ), and Gaffard [31] (HAZ) respectively. Dislocation densities within the weld material were qualitatively reported by Watanabe et al.[25] as significantly higher than for the parent material. Table 3 contains the microstructural values utilised from these sources as detailed, except in the case of the dislocation densities, where values are estimated from within an expected range.

### *3.5. Identification of coarsening rates*

The thermal coarsening rate constants  $K_i$  for both MX and  $M_{23}C_6$  precipitates are identified based on thermal aging data from the grip region of a creep test specimen of Hald et al. [8]. Figure 9 shows a comparison between the thermal coarsening data at 650 °C and Equation (5) while  $\Phi_i$  is set to zero. Utilising these identified values of  $K_i$ , in combination with gage section data from the same creep tests, the strain-induced coarsening constant  $\Phi_i$  has also been identified [5]. Figure 9 also shows resulting comparison with the creep aging data of Hald et al. [8] at 650 °C; a similar quality of fit was achieved for 600 °C [5]. In this paper, precipitate coarsening is assumed to be independent of material zone, as limited data is available on precipitate coarsening kinematics in weld and HAZ materials. Table 4 shows a summary of the identified coarsening rate constants for the  $M_{23}C_6$  carbides and the MX precipitates.

### 3.6. Numerical Modelling

The model has previously been validated for a P91 parent material at 600 and 650 °C [5]. Figure 10 (a) shows the notched tensile specimen geometry and converged mesh from Abaqus™ developed for this calibration. Figure 10 (b) shows the cavitation damage contours, for these conditions, at failure after 1186 hours creep exposure. Failure was deemed to have occurred when an integration point reached a cavitation damage ( $D_{CV}$ ) value of 1. Validation was then performed for a net section nominal stress of 82 MPa at the same temperature, of 650 °C. Figure 11 shows a comparison of the resulting predicted and experimental [21] rupture lives for notched and plain specimens, across a range of stress. Clearly, the rupture life predictions correlate closely to the measured lives across the stress range of interest here.

## 4. Evaluation of precipitate microstructure effects in welded connections

Figure 12 shows the predicted evolution of  $M_{23}C_6$  precipitate diameter for the axisymmetric cross weld geometry for an applied load of 70 MPa at 650 °C, up to the time to failure of 1150 hr. Although the weld material initially has the largest  $M_{23}C_6$  precipitate diameter, the HAZ region experiences the most dramatic increase. The strain concentration within the HAZ leads to enhanced precipitate coarsening which accelerates the formation of creep cavities once precipitates exceed a critical size of about 250 nm. This is consistent with experimental observations of enhanced cavity formation adjacent to large coarsened carbides [12,25,36].

Figure 13 shows the predicted evolution of cavitation damage for an applied stress of 70 MPa. A concentration of cavitation damage occurs at the centre of the HAZ, slightly biased towards the parent material. Cavitation-induced failure within the HAZ is due to high strain accumulation and stress triaxiality occurring within this region, as observed by Watanabe et al. [25] where high levels of stress triaxiality, due to the geometry of the welded connection, is a contributor to Type IV failure.

Figure 14 shows the evolution of triaxiality along the path of highest cavitation damage within the HAZ. The triaxiality is greater near the central axis leading to concentration of damage on this axis and hence cracking is predicted to initiate here.

Figure 15 and Figure 16 show the predicted evolutions of  $M_{23}C_6$  and MX diameters for sample points A, B and C in the PM, HAZ, and WM regions respectively. In Figure 15, the parent material  $M_{23}C_6$  carbides remain the smallest until failure, while the HAZ carbides grow rapidly, reaching the proposed 250 nm [9] threshold mentioned above for enhanced cavitation. Weld material carbides are predicted to be the most stable, coarsening slower than carbides in either parent or HAZ materials. The effect of stress on HAZ precipitate coarsening is demonstrated in Figure 17. A 33% increase in stress is predicted to lead to approximately 87% reduction in the time to reach an  $M_{23}C_6$  diameter of 250 nm, i.e. a highly non-linear response due to combined strain and thermal coarsening effects of Equation (5). In contrast, Figure 16 demonstrates the stability of the MX precipitates in all three materials by their approximately flat coarsening curves for the short term 70 MPa tests. Thermally-induced coarsening dominates the growth characteristics of MX precipitates, as such short-term, high stress testing induces only minor coarsening of this family of precipitates.

## 5. Discussion

Figure 18 shows a close correlation between the multi-precipitate three material model with the parent material and cross-weld test data compiled by Tabuchi et al. [37] and Kimura and Takahashi [38], for 9Cr steels in a wide stress range at 650 °C. The model clearly captures the significant decrease in time to failure due to the weldment; a key objective of the present work. An overestimation of life for PM data is observed at high stress levels, however as this is above plant operational range it is perhaps of less interest to plant operators. The HAZ material parameters were calibrated for 93 MPa test data and the weld material parameters

from tests at 100 MPa and 93 MPa. Based on these calibration conditions accurate stress-life predictions have been achieved for welded connections across a much wider stress range. This demonstrates the predictive capability of the hyperbolic sine based modelling approach for welded 9Cr creep behaviour. Creep tests are extremely time intensive and have high cost associated with them; by utilising the model presented here, accurate long-term predictions can be generated based on short-term, low-cost laboratory tests. The results in Figure 18 can now be used to investigate the weld strength reduction factor (WSRF). The WSRF is calculated according to ASME standards [39] and, for a particular time to failure, it is the ratio of the stress for the cross weld to the corresponding stress for the parent material ( $WSRF = \sigma_{R,CW}/\sigma_{R,PM}$  when  $t_{R,CW} = t_{R,PM}$ ). Typical values here are in the range 0.6 to 0.8 and these have been calculated for both the experimental data and the model results. Figure 19 then shows the ratio of the model-predicted and measured WSRF values ( $WSRF_{\text{predict}}/WSRF_{\text{test}}$ ), it is seen that the model is conservative relative to the experimental data across the range of rupture times.

The model provides a predictive capability for welded component remaining life based on the evolved precipitate microstructure for a 9Cr steel component. Within this framework, the experimentally observed evolution of the microstructure experiencing creep has been predicted using a CDM multi-scale approach. The use of a CDM approach allows for the future addition of other microstructural degradation effects such as oxidation or fatigue loading effects with relative ease.

Ogata et al. [40] performed cross-weld creep tests and welded pipe rupture tests using internal pressure with failure occurring in the HAZ. Creep voids were detected using detailed SEM observations. The number of voids per unit area was highest in the midsection of the HAZ region for both the tensile cross-weld specimen and in the mid-thickness of the pipe.

Using FE simulations Ogata et al. [41] predicted high triaxiality at locations where tests showed a high density of creep voids. Micro-cracks formed from the individual cavities at the mid-thickness of the pipe specimen, growing towards the outer surface of the pipe. The present model predicts cavitation damage inducing failure at the midsection of the HAZ region where the triaxiality is high (see Figure 14). This is in line with the observations of Ogata et al. [40] and also similar to failures observed by Watanabe et al. [42].

While MX precipitates coarsen considerably slower than  $M_{23}C_6$  precipitates, their contribution to the creep strength of the material, via extensive dislocation pinning, is significant. The addition of the MX coarsening kinematics to the model allows for the consideration of compositional variations on the time to failure of the material, i.e. modelling of P91 variants with different MX volume fractions [5].

As Figure 12 and Figure 15 show, the highest rate of  $M_{23}C_6$  precipitate coarsening occurs within the HAZ region. Examining the carbide evolution plot in Figure 12 shows that although coarsening concentration is focused in the centre of the HAZ, this concentration of high precipitate diameter extends across much of the section.

The parameter identification procedure presented here for the HAZ material is necessarily based on some simplifying assumptions. For example, the HAZ region is considered as a single homogeneous material while in fact, it is a more complex heterogeneous structure; consisting of the coarse-grain, fine-grain and inter-critical HAZ regions as shown schematically in Figure 2. Nevertheless, it is argued that the approach used here enables a reasonably accurate initial estimate of the HAZ material behaviour. The extraction of separate creep time curves for coarse grain, fine grain and inter-critical HAZ regions has proven challenging, as these are extremely narrow regions within the material. Some success has been achieved in the identification of creep properties of the various HAZ regions using

indentation creep tests with small indenters, e.g. see Hyde et al [43]. In that work, two distinct material regions within the HAZ material were characterised as high temperature and low temperature HAZ and these regions corresponding to HAZ adjacent to the weld and parent material, respectively. Combining data from this type of testing with the strain compatibility approach described here could potentially produce a more refined modelling approach.

## **6. Conclusions**

Welded component life predictions have been calculated utilising a novel temperature- and strain-induced precipitate coarsening model, including both  $M_{23}C_6$  and MX precipitate families in 9Cr steels, within a CDM creep model. This approach predicts welded component life for a relatively wide stress range, ranging from typical laboratory test conditions to next generation ultra-super critical plant conditions.

A parameter identification methodology previously presented for parent material was extended and applied here to the weld and HAZ materials utilising published microstructural observations. The model has been expanded to include multi-axial effects, with calibration and validation against notched bar test data.

Strain-induced coarsening is predicted to primarily affect  $M_{23}C_6$  precipitates during creep which, when coarsened, enhance the rate of cavitation damage accumulation. An inhomogeneous distribution of  $M_{23}C_6$  diameter has been predicted within the HAZ region of a 9Cr steel weldment. The combined effects of high triaxiality, creep strain and precipitate coarsening accelerate the damage accumulation within the HAZ region leading to failure.

The inclusion of MX precipitate evaluation in the model, allows for compositional effects to be included. This can be coupled, in future work with thermodynamic simulations for

precipitate formation during heat treatments and manufacturing processes (e.g. welding), to predict through process component times to failure.

Two methods of increasing the life of welded components are suggested from this work, (i) reducing the initial carbide diameter within the HAZ region via careful heat treatment, and (ii) enhancing the thermal stability of precipitates by addition of new stabilising elements during manufacture and welding. One such example is the novel 9Cr material, MarBN, manufactured with controlled addition of boron and nitrogen to enhance the thermal stability of precipitates and retain the hierarchical microstructure of the parent material post-weld.

### **Acknowledgements**

This publication has emanated from research conducted with the financial support of (i) the Irish Research Council under Project Number GOIPG/2015/3944 and (ii) Science Foundation Ireland as part of the MECHANNICS joint project between NUI Galway and University of Limerick under Grant Number SFI/14/IA/2604.

### **References**

- [1] Abson DJ, Rothwell JS. Review of Type IV cracking of weldments in 9-12%Cr creep strength enhanced ferritic steels. *Int Mater Rev* 2013; 56: 437–473.
- [2] Farragher TP, Scully S, O’Dowd NP, et al. Development of life assessment procedures for power plant headers operated under flexible loading scenarios. *Int J Fatigue* 2013; 49: 50–61.
- [3] Maruyama K, Sawada K, Koike J. Strengthening mechanisms of creep resistant tempered martensitic steel. *ISIJ Int* 2001; 41: 641–653.
- [4] Barrett RA, O’Donoghue PE, Leen SB. A dislocation-based model for high temperature cyclic viscoplasticity of 9–12Cr steels. *Comput Mater Sci* 2014; 92: 286–297.
- [5] Ó Murchú C, Leen SB, O’Donoghue PE, et al. A physically-based creep damage model for effects of different precipitate types. *Mater Sci Eng A* 2017; 682: 714–722.
- [6] Orowan E. Problems of plastic gliding. *Proc Phys Soc* 1940; 52: 9–22.

- [7] Panait CG, Zielińska-Lipiec A, Koziel T, et al. Evolution of dislocation density, size of subgrains and MX-type precipitates in a P91 steel during creep and during thermal ageing at 600C for more than 100,000h. *Mater Sci Eng A* 2010; 527: 4062–4069.
- [8] Hald J, Korcakova L. Precipitate stability in creep resistant ferritic steels-experimental investigations and modelling. *ISIJ Int* 2003; 43: 420–427.
- [9] Taneike M, Kondo M, Morimoto T. Accelerated Coarsening of MX Carbonitrides in 12%Cr Steels during Creep Deformation. *ISIJ Int* 2001; 41: S111–S115.
- [10] Hättestrand M, Andrén H-O. Influence of strain on precipitation reactions during creep of an advanced 9% chromium steel. *Acta Mater* 2001; 49: 2123–2128.
- [11] Cane BJ. Creep fracture of dispersion strengthened low alloy ferritic steels. *Acta Metall* 1981; 29: 1581–1591.
- [12] Lee JS, Maruyama K. Mechanism of microstructural deterioration preceding type IV failure in weldment of Mod.9Cr-1Mo steel. *Met Mater Int* 2015; 21: 639–645.
- [13] Hald J. Microstructure and long-term creep properties of 9–12% Cr steels. *Int J Press Vessels Pip* 2008; 85: 30–37.
- [14] Sawada K, Taneike M, Kimura K, et al. Effect of nitrogen content on microstructural aspects and creep behavior in extremely low carbon 9Cr heat-resistant steel. *ISIJ Int* 2004; 44: 1243–1249.
- [15] Paul VT, Saroja S, Hariharan P, et al. Identification of microstructural zones and thermal cycles in a weldment of modified 9Cr-1Mo steel. *J Mater Sci* 2007; 42: 5700–5713.
- [16] Arivazhagan B, Prabhu R, Albert SK, et al. Microstructure and Mechanical Properties of 9Cr-1Mo Steel Weld Fusion Zones as a Function of Weld Metal Composition. *J Mater Eng Perform* 2009; 18: 999–1004.
- [17] Vijayalakshmi M, Saroja S, Paul VT, et al. Microstructural zones in the primary solidification structure of weldment of 9Cr-1Mo steel. *Metall Mater Trans A* 1999; 30: 161–174.
- [18] Abaqus Analysis User's Manual (6.14).
- [19] Dyson BF, Osgerby S. *Modelling and Analysis of creep deformation and fracture in a 1 Cr 1/2 Mo Ferritic Steel*. Research DMM(A)116, The National Physical Laboratory, August 1993.
- [20] Perrin IJ, Hayhurst DR. Creep constitutive equations for a 0.5Cr–0.5Mo–0.25V ferritic steel in the temperature range 600–675°C. *J Strain Anal Eng Des* 1996; 31: 299–314.
- [21] Hyde TH, Becker AA, Sun W, et al. Finite-element creep damage analyses of P91 pipes. *Int J Press Vessels Pip* 2005; 83: 853–863.
- [22] Oruganti R, Karadge M, Swaminathan S. Damage mechanics-based creep model for 9–10%Cr ferritic steels. *Acta Mater* 2011; 59: 2145–2155.

- [23] Dyson B. Use of CDM in materials modelling and component creep life prediction. *Trans-Am Soc Mech Eng J Press Vessel Technol* 2000; 122: 281–296.
- [24] Roters F, Raabe D, Gottstein G. Work hardening in heterogeneous alloys—a microstructural approach based on three internal state variables. *Acta Mater* 2000; 48: 4181–4189.
- [25] Watanabe T, Tabuchi M, Yamazaki M, et al. Creep damage evaluation of 9Cr–1Mo–V–Nb steel welded joints showing Type IV fracture. *Int J Press Vessels Pip* 2006; 83: 63–71.
- [26] Hyde TH, Sun W, Becker AA, et al. Creep properties and failure assessment of new and fully repaired P91 pipe welds at 923K. *Proc Inst Mech Eng Part J Mater Des Appl* 2004; 218: 211–222.
- [27] Haney EM, Dalle F, Sauzay M, et al. Macroscopic results of long-term creep on a modified 9Cr–1Mo steel (T91). *Mater Sci Eng A* 2009; 510–511: 99–103.
- [28] Agyakwa P. *Creep and microstructural development in P91 weldments at elevated temperature*. PhD, University of Nottingham, 2004.
- [29] Spigarelli S, Quadrini E. Analysis of the creep behaviour of modified P91 (9Cr–1Mo–NbV) welds. *Mater Des* 2002; 23: 547–552.
- [30] Barrett RA. *Experimental Characterisation and Computational Constitutive Modelling of High Temperature Degradation in 9Cr Steels Including Microstructural Effects*. PhD, National University of Ireland, Galway, 2016.
- [31] Gaffard V. *Experimental study and modelling of high temperature creep flow and damage behaviour of 9Cr1Mo-NbV steel weldments*. PhD, Ecole Des Mines De Paris, 2004.
- [32] Milović L, Vuherer T, Blačić I, et al. Microstructures and mechanical properties of creep resistant steel for application at elevated temperatures. *Mater Des* 2013; 46: 660–667.
- [33] Abd El-Azim ME, Nasreldin AM, Zies G, et al. Microstructural instability of a welded joint in P91 steel during creep at 600°C. *Mater Sci Technol* 2005; 21: 779–790.
- [34] Barbadikar DR, Deshmukh GS, Maddi L, et al. Effect of normalizing and tempering temperatures on microstructure and mechanical properties of P92 steel. *Int J Press Vessels Pip* 2015; 132–133: 97–105.
- [35] Vivier F, Gourgues-Lorenzon A-F, Besson J, et al. Metallurgical properties and creep behaviour of a grade 91 steel base metal and weldment after short-term exposure at 500° C. In: *ECCC Conference on Creep and Fracture in High Temperature Components, Design and Life Assessment Issues, Dübendorf (Zürich)* <http://www.ommi.co.uk/PDF/Articles/204.pdf> (2009, accessed 15 September 2017).
- [36] Matsui M, Tabuchi M, Watanabe T, et al. Degradation of Creep Strength in Welded Joint of 9%Cr Steel. *ISIJ Int* 2001; 41: 126–130.

- [37] Tabuchi M, Takahashi Y. Evaluation of creep strength reduction factors for welded joints of modified 9Cr-1Mo steel. *J Press Vessel Technol* 2012; 134: 031401.
- [38] Kimura K, Takahashi Y. Evaluation of long-term creep strength of ASME grade 91, 92, and 122 type steels. In: *ASME Paper No. PVP2012-78323*. Toronto, Ontario, Canada: American Society of Mechanical Engineers, 2012.
- [39] *ASME Boiler & Pressure Vessel Code*. Section III, Division 1, Subsection NH, New York: American Society of Mechanical Engineers, 2004.
- [40] Ogata T, Sakai T, Yaguchi M. Damage assessment method of P91 steel welded tube under internal pressure creep based on void growth simulation. *Int J Press Vessels Pip* 2010; 87: 611–616.
- [41] Ogata T, Sakai T, Yaguchi M. Damage characterization of a P91 steel weldment under uniaxial and multiaxial creep. *Mater Sci Eng A* 2009; 510–511: 238–243.
- [42] Watanabe T, Tabuchi M, Yamazaki M, et al. Creep damage evaluation of 9Cr–1Mo–V–Nb steel welded joints showing Type IV fracture. *Int J Press Vessels Pip* 2006; 83: 63–71.
- [43] Hyde TH, Sun W. Determining High Temperature Properties of Weld Materials. *Solid Mech Mater Eng Int Ser A* 2000; 43: 40–414.
- [44] MacArghail P. Schematic of HAZ microstructures.

Tables

**Table 1. Identified creep parameters for the three material zones in a 9Cr cross weld specimen.**

Materials	$\dot{\epsilon}_0$ (hr <sup>-1</sup> )	$h$ (MPa)	$H^*$ (-)	$C$ (-)	$\nu$ (-)
PM	$6 \times 10^{13}$	7919	0.09	2.5	3.8
HAZ	$1.02 \times 10^{12}$	2904	0.25	10	3.8
WM	$1.88 \times 10^{13}$	862	0.52	1.125	3.8

**Table 2. Dimensions of cross-weld specimen utilised for HAZ creep strain versus time curve extrapolation [28].**

Section	Dimension (mm)
Parent material ( $L_{PM}$ )	7.75
Heat affected zone ( $L_{HAZ}$ )	2.25
Weld metal ( $L_{WM}$ )	6
Specimen diameter ( $\varnothing D$ )	8.66

**Table 3. Microstructural model inputs and parameters for the three material zones.**

Materials	$d_{M23C6,0}$ (nm)	$d_{MX,0}$ (nm)	$f_{M23C6}$ (%)	$f_{MX}$ (%)	$\lambda_{ob}$ (nm)	$w$ ( $\mu m$ )	$d_g$ ( $\mu m$ )	$\rho$ (m <sup>-2</sup> )
PM	100	36	2	0.1	38	0.4	40	$3.66 \times 10^{14}$
HAZ	128	65	0.002	0.001	65	4	12	$2.1 \times 10^{14}$
WM	200	55	0.05	0.0001	55	5	140	$2.4 \times 10^{14}$

**Table 4. Identified coarsening rates for  $M_{23}C_6$  and MX families of precipitates**

Materials	$K_{M23C6}$ (mm <sup>3</sup> hr <sup>-1</sup> )	$K_{MX}$ (mm <sup>3</sup> hr <sup>-1</sup> )	$\Phi_{M23C6}$ (mm <sup>3</sup> )	$\Phi_{MX}$ (mm <sup>3</sup> )
PM, HAZ, WM	$6.35 \times 10^{-15}$	$3.9 \times 10^{-18}$	$1.04 \times 10^{-9}$	$1.18 \times 10^{-14}$

## Figures

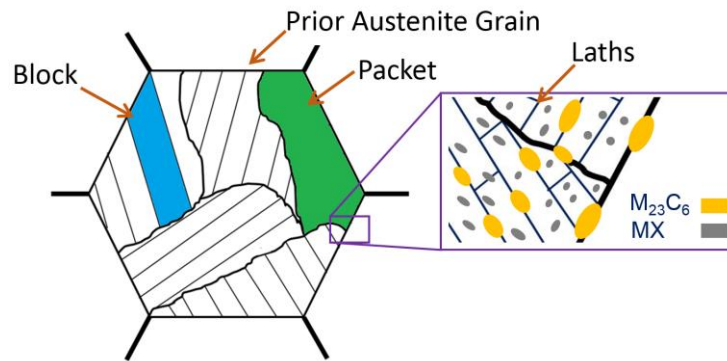


*Figure 1. Schematic of 9Cr steel hierarchical microstructure [5].*

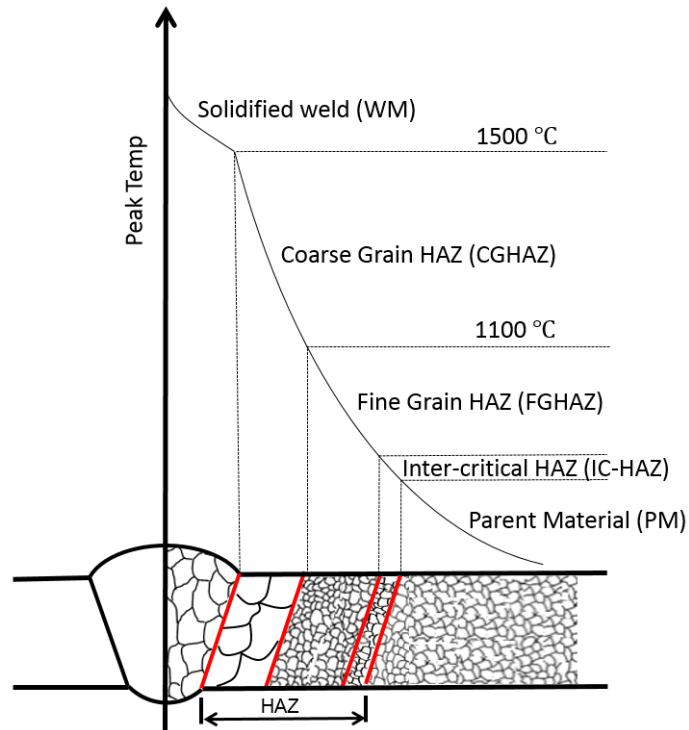


*Figure 2. Microstructure gradient within a typical weldment of 9Cr steel, showing distinct regions within HAZ as a function of peak temperature [44].*

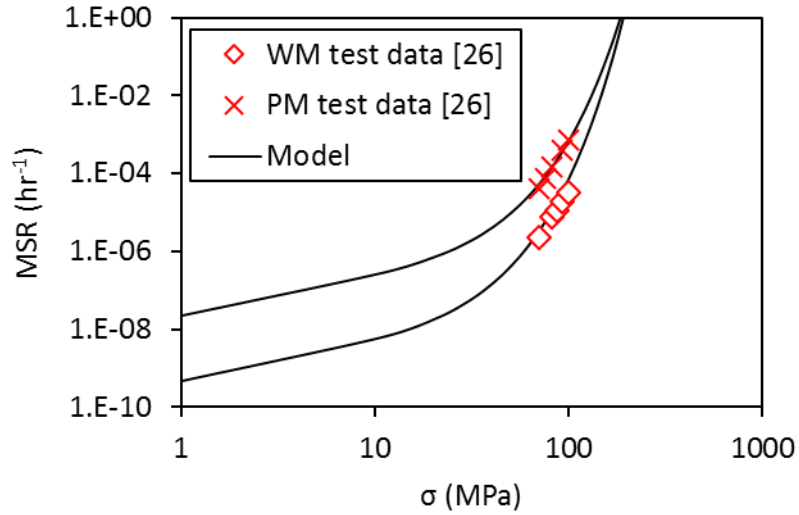


**Figure 3. Comparison of predicted minimum creep strain rate with measured data from Hyde et al. [26] for parent and weld material**

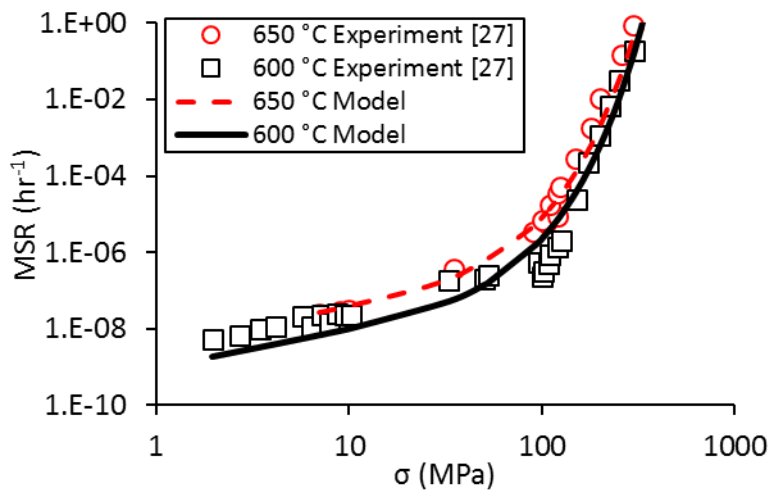


**Figure 4. Comparison MSR equation against experimental data for P91 parent material at 600 °C and 650 °C.**

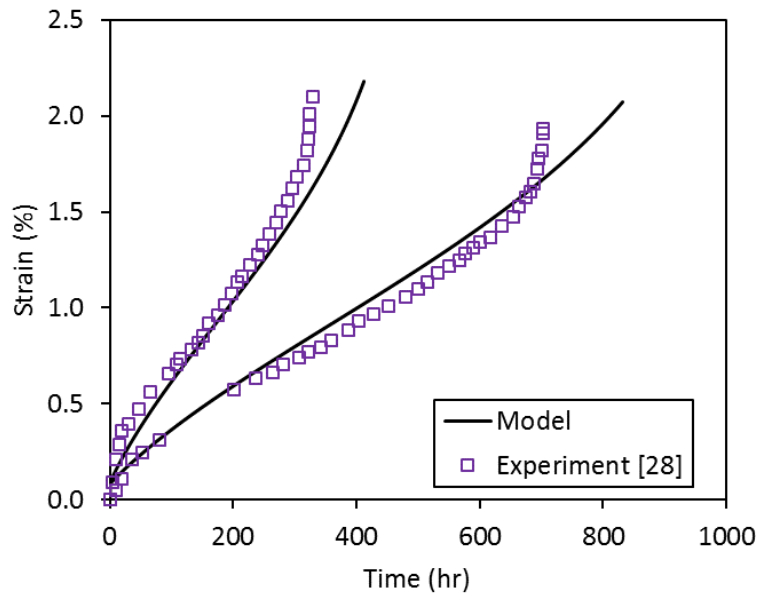


*Figure 5. Model fit to experimental data at 650 °C for 9Cr weld material. Test data obtained from Agyawka [28].*

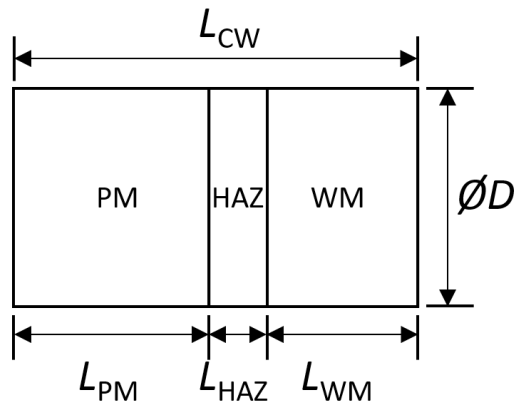


*Figure 6. Schematic of the three-material gage length of CW specimen used in [26] and [28], dimensions in Table 2.*

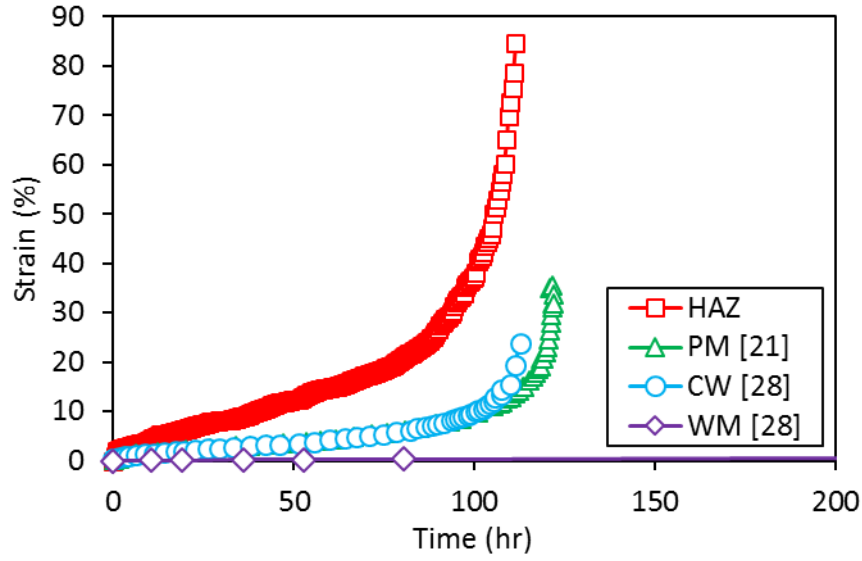


**Figure 7. Results of the creep strain extraction methodology for the HAZ region compared with the three data sets, PM, WM and cross-weld utilised in Equation (12). Test data from Agyawka [28] and Hyde et al. [21] for Bar 257 tested at 93 MPa and 650 °C.**

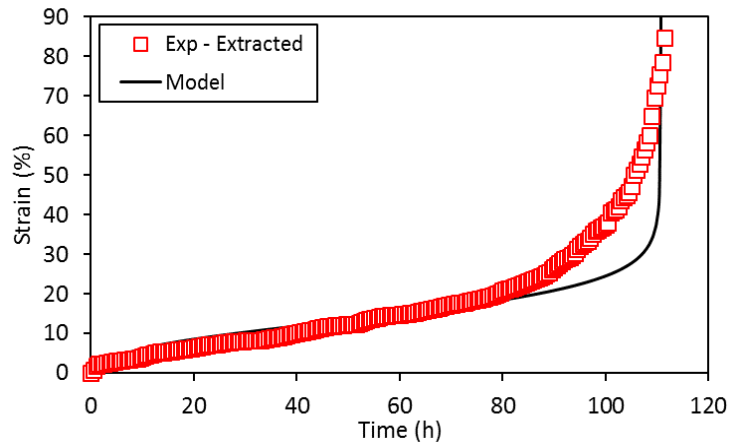


**Figure 8. Comparison of predicted and measured HAZ creep response for 93 MPa and 650 °C.**

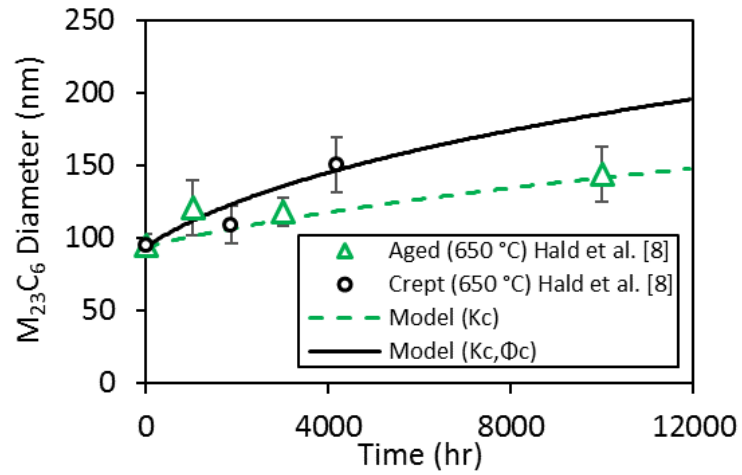


**Figure 9. Identification of strain and temperature induced coarsening parameters based on creep and thermal aging data at 650 °C from Hald et al. [8].**

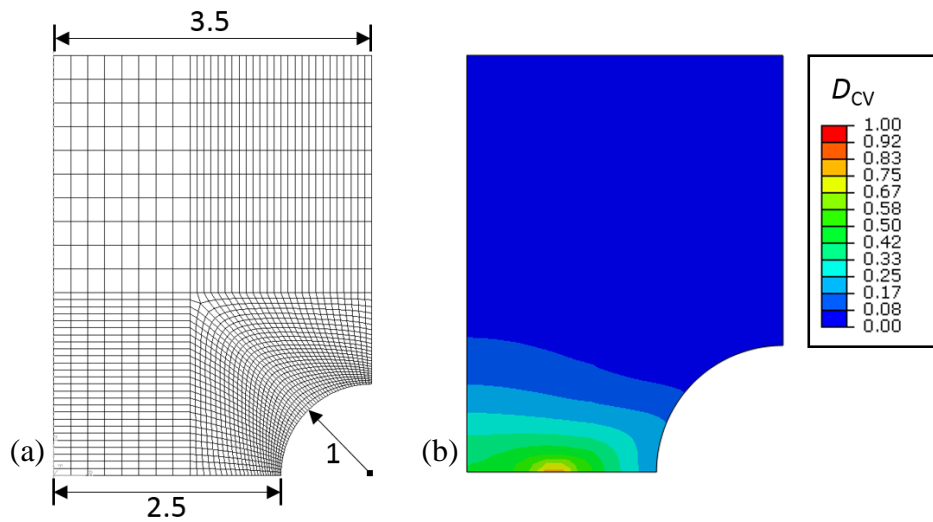


**Figure 10. Notched bar FE model geometry showing (a) Converged mesh with dimensions in mm and (b) cavitation damage contour at failure for nominal section stress of 93 MPa at 650 °C, time to failure is 2011 hrs.**

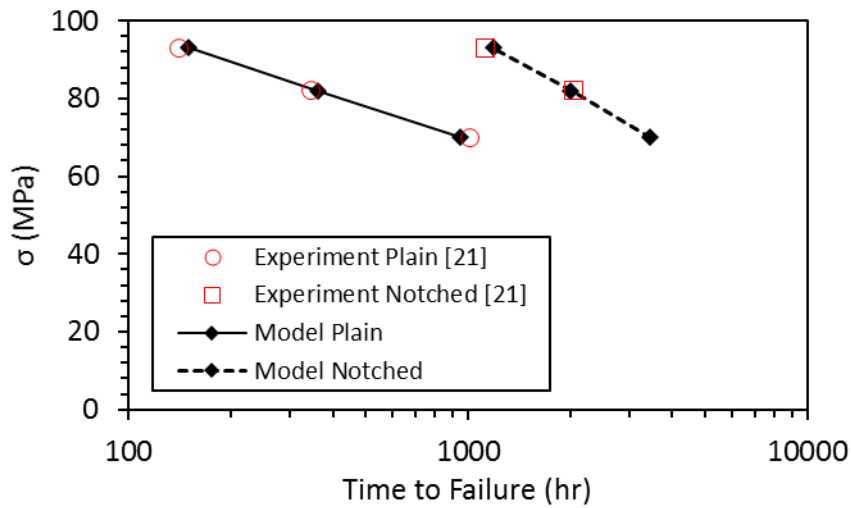


Figure 11. Comparison of predicted and measured creep rupture stress-time responses for plain and notched bar tensile tests at 650°C.

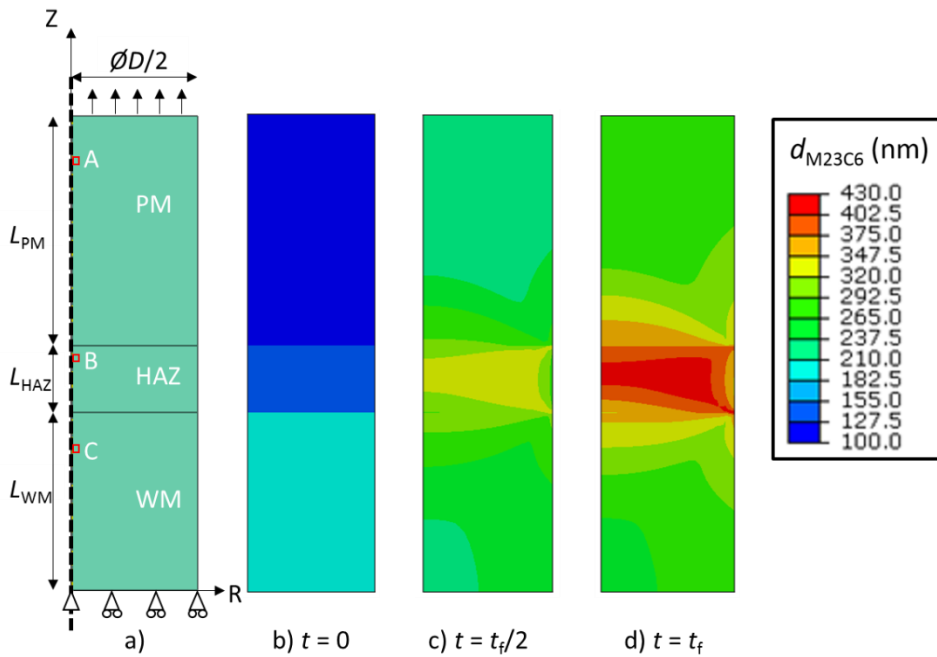
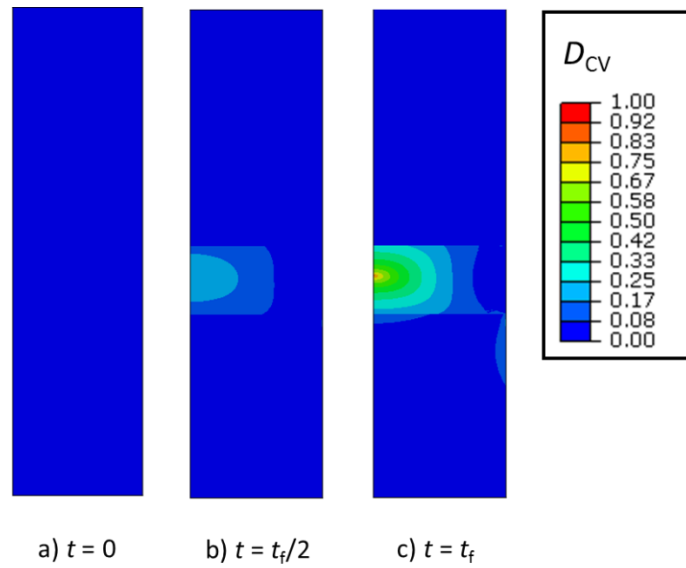
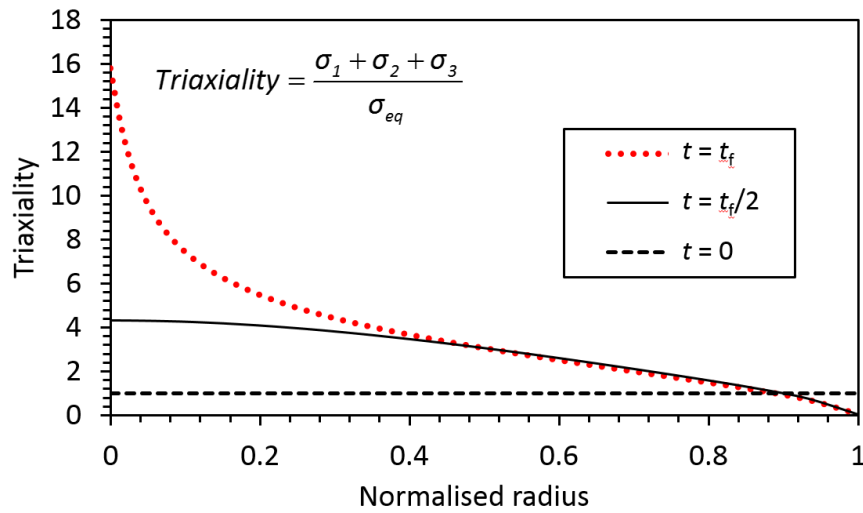


Figure 12. Schematic of assumed cross-weld geometry and predicted evolution of associated distributions of  $M_{23}C_6$  precipitate diameter for 70 MPa at 650°C, up to failure at 1150 hrs.



**Figure 13.** Cavitation damage evolution for a load of 70 MPa at 650 °C. Maximum damage accumulates within the HAZ region leading to failure.



**Figure 14.** Evolution of radial distribution of stress triaxiality, across the centre of HAZ, for an applied load of 70 MPa at 650 °C. Maximum triaxiality occurs at the central axis in the HAZ where failure is predicted to occur.

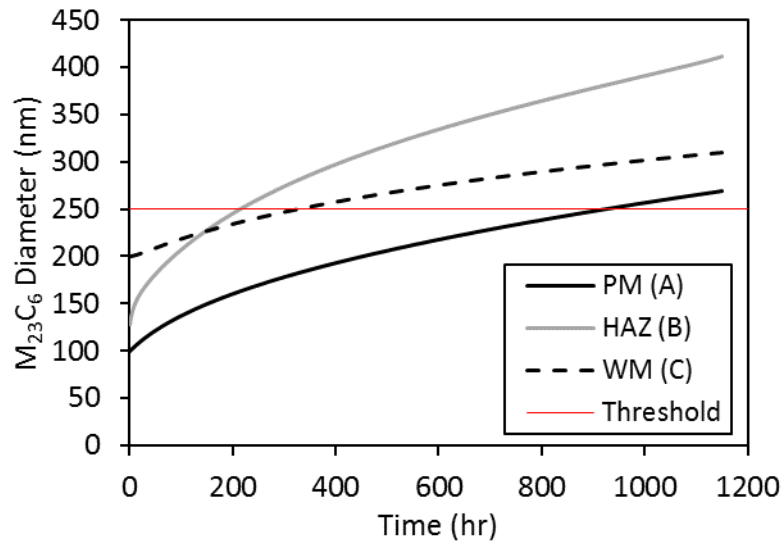


**Figure 15.** Predicted evolutions of  $M_{23}C_6$  diameter for parent, weld and HAZ materials for 70 MPa case, at points A, B and C in Figure 12.

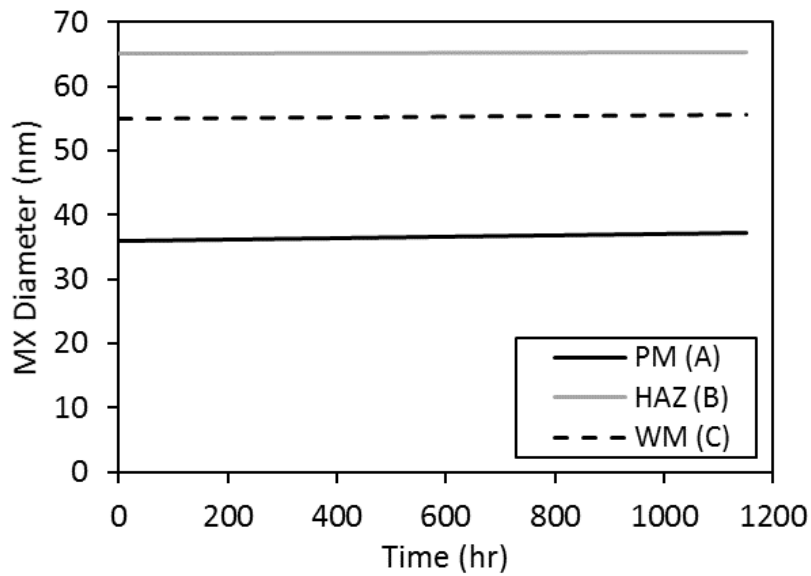


**Figure 16.** Predicted evolutions of MX diameter for parent, weld and HAZ materials for 70 MPa case at points A, B, C, in Figure 12.

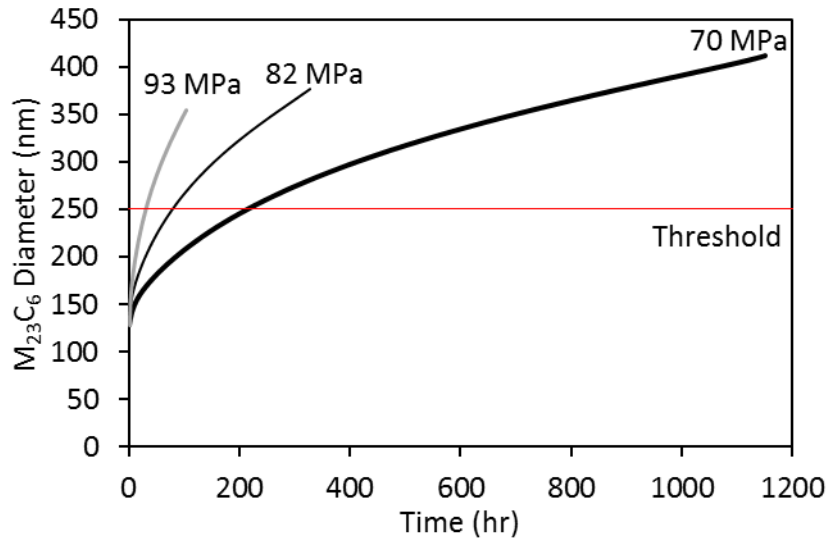


*Figure 17. Predicted effect of stress on  $M_{23}C_6$  the precipitate coarsening dynamics within the HAZ region at point B, in Figure 12.*

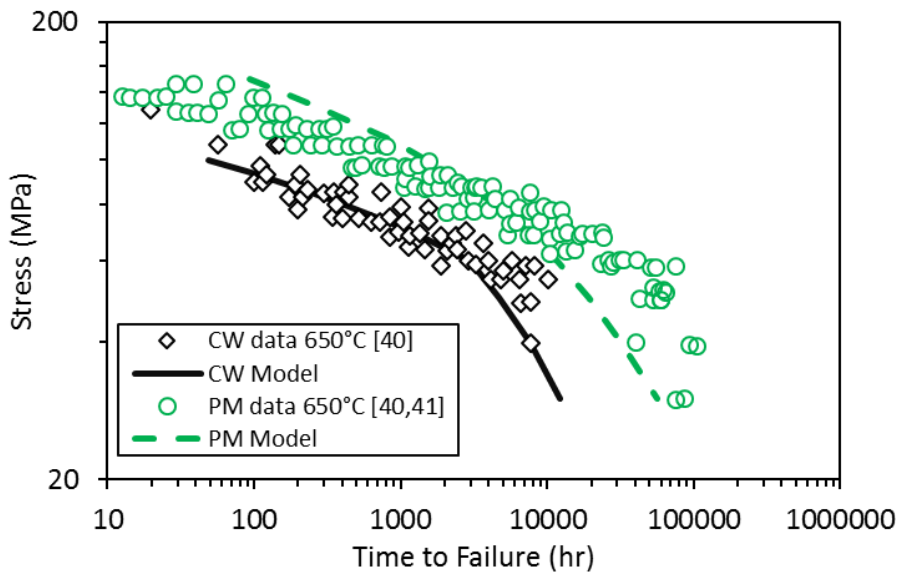


*Figure 18. Comparison between experimental data for P91 parent and cross weld specimens at 650 °C, from Tabuchi and Takahashi [37] and Kimura et al.[38] with model results.*

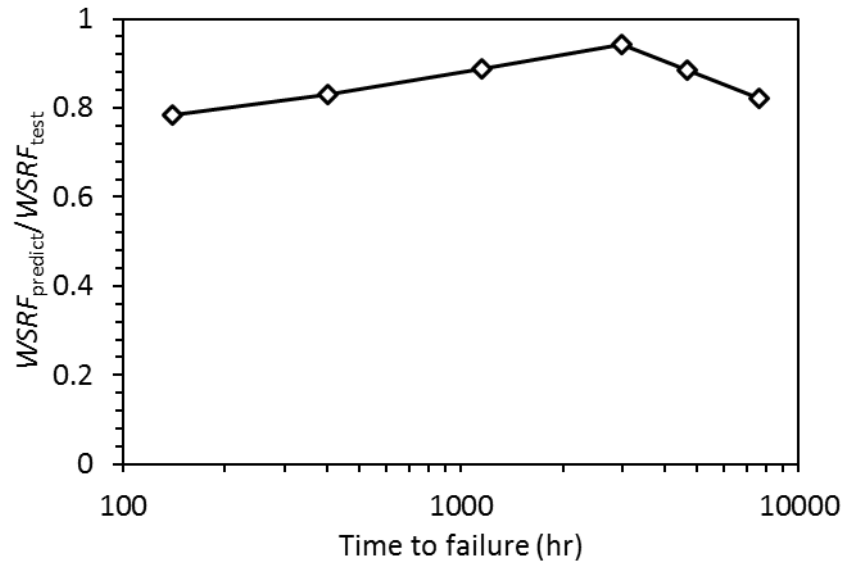


*Figure 19. Ratio of model predicted WSRF's to experimental WSRF's [37] for a range of failure lives, calculated per ASME standards [39].*